Scanning Microscopy Vol. 11, 1997 (Pages 67-80) 0891-7035/97$5.00+.25
Scanning Microscopy International, Chicago (AMF O'Hare), IL 60666 USA

PHASE-RETRIEVAL X-RAY MICROSCOPY BY WIGNER-DISTRIBUTION DECONVOLUTION: SIGNAL PROCESSING

Henry N. Chapman

Department of Physics, SUNY at Stony Brook, Stony Brook, NY

Abstract

Phase and amplitude images have been reconstructed from data collected in a scanning transmission x-ray microscope by applying the method of Wigner-distribution deconvolution. This required collecting coherent microdiffraction patterns at each point of a two-dimensional scan of an object and then deconvolving the four-dimensional Wigner-distribution function of the lens from the data set. The process essentially analyses the interference which occurs in the microdiffraction plane and which modulates as the object is scanned. The image-processing steps required to deconvolve experimental data are described. These steps result in the reconstructions of diffraction-limited phased images, to a spatial-frequency cut-off of 1/45 nm^{-1}. The estimated accuracy of the images is 0.05 rad in phase and 10% in amplitude. Data were collected at an x-ray wavelength of 3.1 nm.

Key Words: X-ray microscopy, phase-retrieval, zone plates, deconvolution, x-ray interferometry.

*Present address and address for correspondence:
Henry N. Chapman
Lawrence Livermore National Laboratory L-395
P.O.Box 808
Livermore, CA 94550

Telephone number: (925) 423 1580
FAX number: (925) 423 1488
E-mail: chapman9@llnl.gov

Introduction

Wigner-deconvolution phase-retrieval microscopy is a new technique for retrieving the phase and amplitude of transmission microscope images (Rodenburg and Bates, 1992; Bates and Rodenburg, 1989). This technique can be employed in a microscope of either the scanning or conventional geometry and allows the formation of superresolved images (Rodenburg and Bates, 1992; Nellist and Rodenburg, 1994). The phase-retrieval and superresolution characteristics of the technique have been demonstrated in scanning transmission microscopes that utilise visible light (McCallum and Rodenburg, 1992), electrons (Rodenburg *et al.*, 1993; Nellist *et al.*, 1995), and soft x-rays (Chapman, 1996). In a scanning microscope the method requires collecting a two-dimensional micro-diffraction pattern (a coherent convergent beam diffraction pattern) at each point in a two-dimensional scan. The ability to retrieve the phase can be interpreted as a self-interferometric process, where two beams travelling in different directions from the objective lens are combined at the specimen and diffracted into a single element of a CCD (charge-coupled device) detector. The intensity modulation resulting from scanning the specimen gives the relative phase of the two diffracted orders. The deconvolution process separates the contributions of all possible pairs of interfering beams.

X-ray microscopes are in use or under development in a number of laboratories for imaging wet, approximately micrometre-thick biological specimens, and materials characterisation, at ~50 nm resolution (Kirz *et al.*, 1995). Both transmission x-ray microscope (TXMs) and scanning transmission x-ray microscopes (STXMs) exist; these are analogous to conventional transmission (CTEM) and scanning transmission (STEM) electron microscopes, respectively. Scanning transmission x-ray microscopes require a highly coherent incident beam, which necessitates the use of a high-brightness x-ray source such as an undulator at a synchrotron facility. All current high-resolution x-ray microscopes use zone plates for the probe- or image-forming objective. These are diffractive optical elements made up of concentric circular zones, and the numerical aperture, and hence the resolution, is limited by the smallest zone width that can be fabricated. Currently,

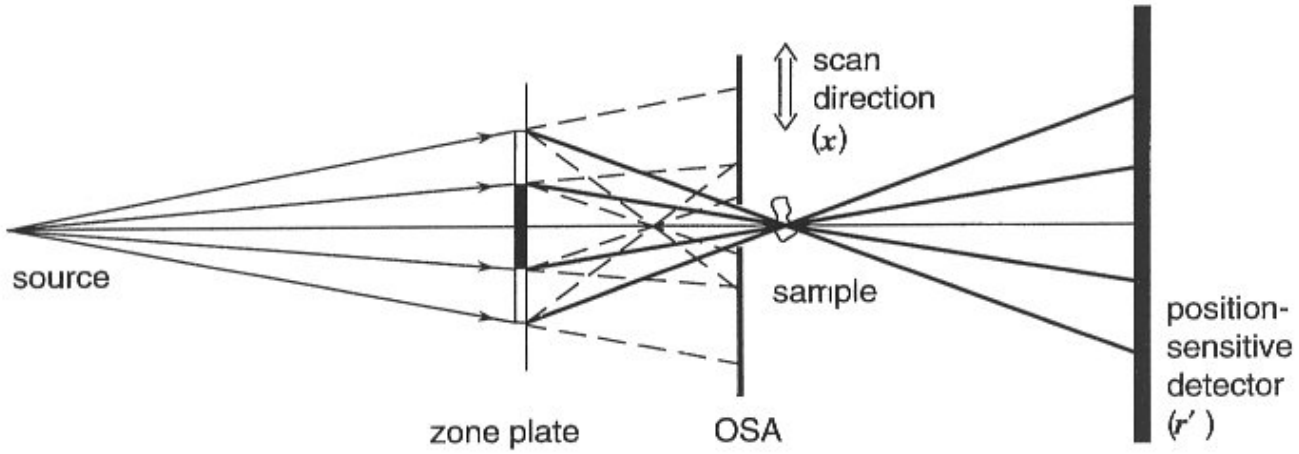

Figure 1. Schematic diagram of an STXM used for collecting microdiffraction data. The annular pupil of the zone plate ensures that at the plane of the first order focus other diffracted orders are annuli (zero and second order are shown as dashed lines). Thus, a small aperture (the OSA) can be used to select only the first order. The position-sensitive detector was a thinned, back-illuminated CCD. The diagram is not to scale: the source (the exit slit of the monochromator) is located about three metres from the zone plate, which has a focal length of about one millimetre.

with electron-beam lithography, zone-plates below 25-nm zone-width have been reported (Thieme *et al.*, 1994). Usually, the mode of operation of STXMs is incoherent bright-field imaging, where the image is a map of the x-ray absorption of the specimen. For wet biological samples, the x-ray wavelength is usually chosen in or near the "water window" between the carbon and oxygen *K*-shell absorption edges (that is, 4.4 to 2.3 nm) so that the contrast between carbon and water is maximised and so that the x-rays penetrate many micrometres of water. Other modes of imaging in the STXM, achieved by varying the detector type or geometry, include dark field (Morrison and Browne, 1992; Chapman *et al.*, 1996), where maps of the elastic scattering are produced; differential phase-contrast (Palmer and Morrison, 1992); and scanning luminescence x-ray microscopy (Jacobsen *et al.*, 1993; von Brenndorff *et al.*, 1995), where the image is formed from x-ray-stimulated visible emission of a dye.

Wigner deconvolution of the data set collected in an x-ray microscope yields a complex-valued, sub-visible-light-resolution image of the specimen's transmission, which in turn depends on the real and imaginary parts of the refractive index of the specimen. This quantitative high-resolution information would be very useful in order to find unambiguous information about the ultrastructure of a specimen, and could offer supplemental information to near-absorption-edge images, where both the amplitude and phase of the transmitted beam vary rapidly with the wavelength and chemical environment. Accurately knowing the complex refractive index of materials in microstructures, such as integrated circuits or diffractive optics, would be extremely beneficial to help diagnose or improve their manufacture or design.

The emphasis of this report is on the image processing required to extract phase maps of specimens from x-ray microdiffraction data collected in the Stony Brook STXM. The instrumentation of the microscope is described in the next section. In the section on "Wigner-Distribution Deconvolution" the theory of Wigner deconvolution, as was first put forward by Rodenburg and Bates (1992), is briefly reviewed. The steps required to carry out the deconvolution on the x-ray data are explained in the section entitled "Deconvolving Sampled Data", using experimental data from the imaging of a transmission grating as an example. Experimental results of non-periodic test objects are given in the section of "Phase-Retrieved Image of a Non-Periodic Object". The phases and amplitudes of the retrieved images were found to be in excellent quantitative agreement with calculated images.

The Stony Brook Scanning Transmission X-Ray Microscope

The Stony Brook STXM operates on the Soft X-ray Undulator beamline at the National Synchrotron Light Source at Brookhaven National Laboratory in the USA; a schematic diagram is shown in Figure 1. The beamline and microscope have been described elsewhere (Jacobsen *et al.*, 1991, 1995). The x-ray source is a soft-x-ray undulator

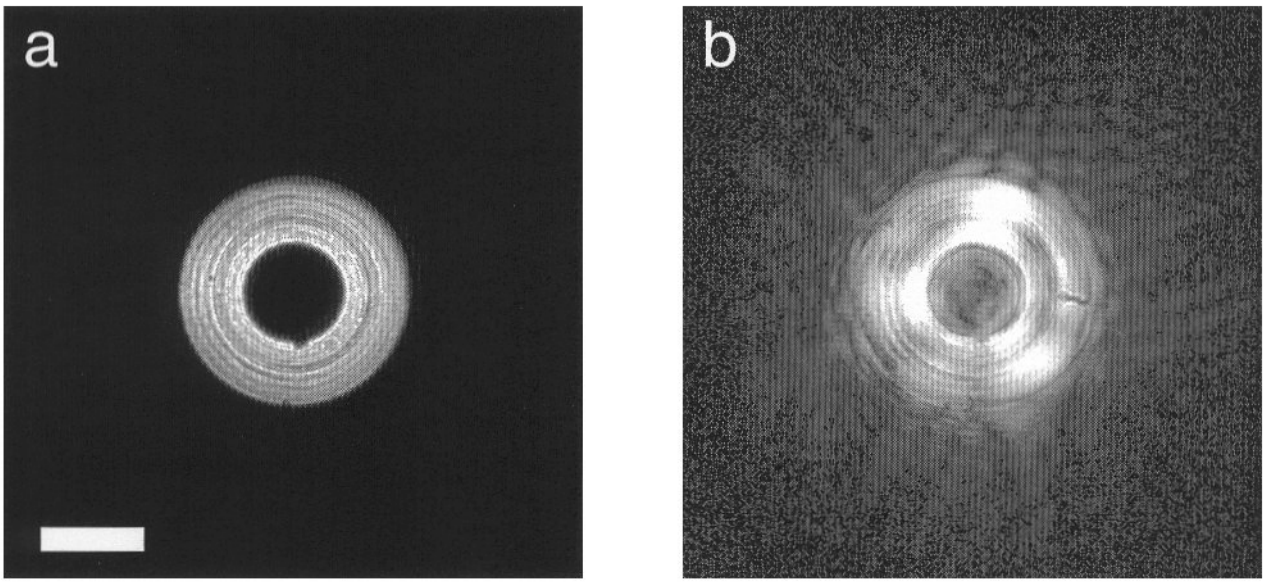

Figure 2. (**a**) Measured microdiffraction pattern with no object in place. This is a measurement of the square of the zone-plate pupil amplitude, $|A(\mathbf{r}')|^2$. The scalebar shows 10 μm^{-1}. (**b**) Measured pattern with a group of 0.5 μm-diameter latex spheres in focus.

which is spatially and temporally filtered by apertures and a grating monochromator (Rarback *et al.*, 1990). The objective lens of the microscope is a Fresnel zone plate. This binary diffractive optical element diffracts the beam into many focal orders. To allow only the first order focus, which is used as the probe, to illuminate the image plane, a zone plate with an annular pupil is used. The far-field diffraction pattern of each order in this case will be an annulus, and at the plane of the first-order focus other orders will be annuli. Placing a small aperture (the order-selecting aperture, or OSA) slightly upstream of the first-order focus will block all orders except for the first.

The zone plate used in all investigations reported here was fabricated using electron-beam lithography by Erik Anderson, now of Lawrence Berkeley National Laboratory Anderson and Kern, 1992). It was 90 μm in diameter, with a 40-μm-diameter central stop, and had an outer zone width of 45 nm (giving a maximum image spatial frequency of 22.2 μm^{-1} for incoherent bright-field imaging at all soft-x-ray wavelengths). The zone plate is designed to have zero spherical aberration when used in the present beamline configuration.

The specimen is scanned across the zone plate focus by a scanning stage that consists of a flexure stage, moved by piezoelectric actuators, which itself is mounted on stepper motor driven stages. The sample and zone plate are located in an air or helium environment.

Microdiffraction patterns are measured with a thinned, back-illuminated CCD which directly detects x rays, as has been documented (Chapman *et al.*, 1995). The CCD used is a SITe chip with 512×512 pixels, spaced at 24-μm intervals. For all data collected here the specimen plane to CCD distance was 75 mm. At a wavelength of 3.2 nm the pixels sample the microdiffraction pattern at 0.10 μm^{-1}.

Microdiffraction data sets are typically collected at a rate of 0.5 to 1.0 s per diffraction pattern (limited by the readout rate of the CCD), so an entire set of 64x64 patterns may take over an hour to collect. When a new sample is placed on the scanning stage, the sample invariably drifts as its temperature equilibrates with its surroundings. It may take an hour before the sample stabilises, but after this time data sets can be collected without the need for drift compensation.

For the method of Wigner distribution deconvolution, the phase and amplitude of the microdiffraction pattern of the zone plate (i.e., the zone-plate pupil function) must be accurately known, as is explained in the next section. The square of the pupil amplitude can easily be measured, and it is found that there are high-spatial-frequency radial errors of high contrast across the pupil (see Figure 2). These have been attributed to errors in the placement of the zones of the zone plate (Chapman *et al.*, 1995; Tejnil *et al.*, 1996). In this case there would be a corresponding pupil phase error. For this work it was assumed that the pupil phase was zero.

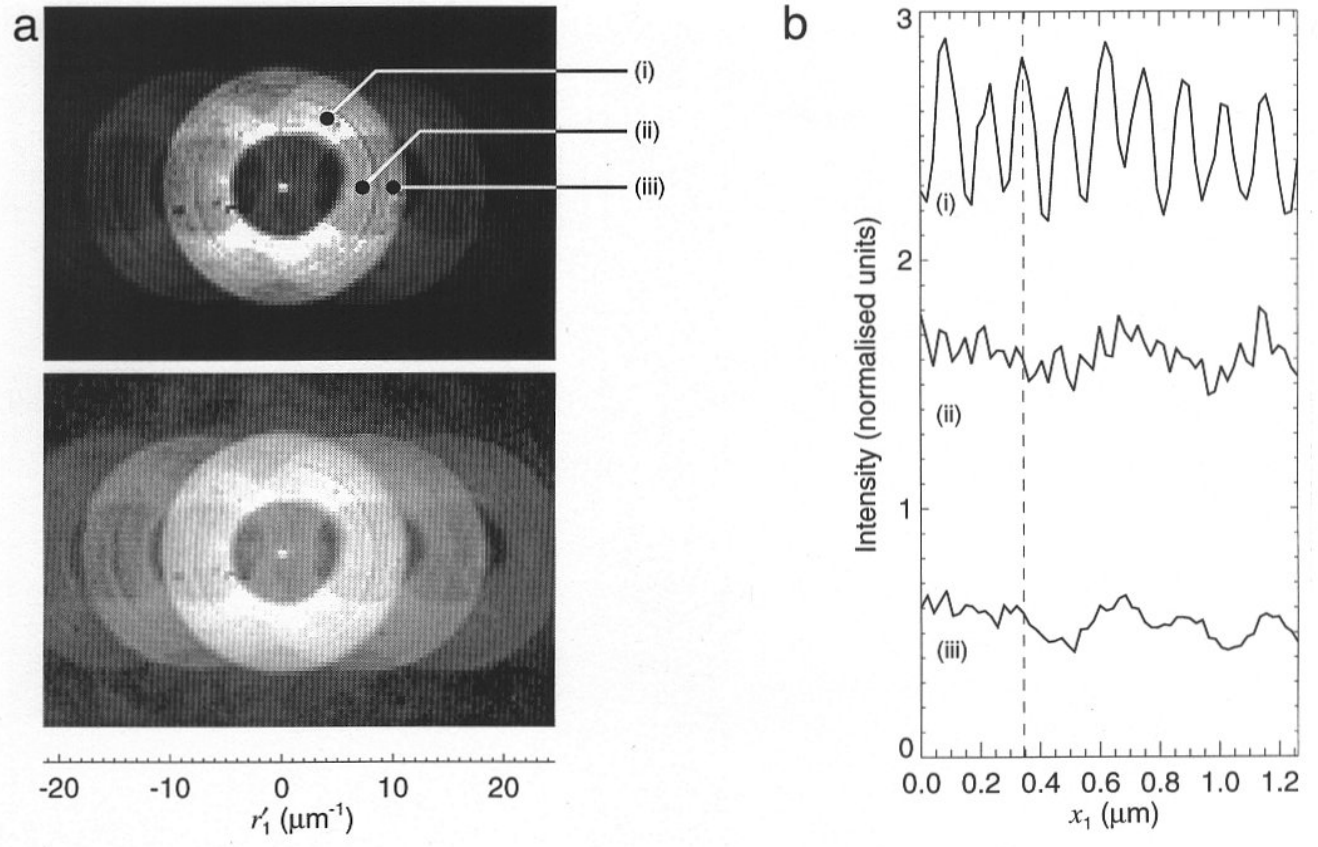

Figure 3. (**a**) One microdiffraction pattern from a data set of a transmission grating object, shown on linear (top) and logarithmic (bottom) greyscales. Each diffracted order of the grating gives rise to a pupil function, and interference between the pupil functions can be seen. The data were recorded at an x-ray wavelength of 3.1 nm. The grating is actually part of another zone plate, although it is examined in only a small field in which the zones appear straight The data set consisted of a one-dimensional scan of 128 samples in real space, spaced by 22.0 nm. Each microdiffraction pattern consisted of 128x128 samples with $\Delta\mathbf{r}' = 0.4\,\mu m^{-1}$. (**b**) Coherent bright-field images extracted from the data set: (i) from a single CCD pixel receiving 0 and +1 orders; (ii) from a pixel receiving only 0 and +2 orders; and (iii) from a region in the 0 order that does not interfere with higher orders. The images have been displaced by one intensity unit for clarity. The pixel positions from which the coherent images were extracted are labelled in (a).

Alternatively, Wigner distribution deconvolution can be used to retrieve the pupil phase, as has been demonstrated (Chapman, 1996).

Wigner-Distribution Deconvolution

The Microdiffraction Data Set

In the following description the notation is used that primed coordinates are defined in reciprocal space and non-primed coordinates are defined in real space. Two-dimensional vectors are written as $\mathbf{r} \equiv (r_1, r_2)$. A two-dimensional Fourier transform will imply forward propagation and an inverse transform will imply backward propagation.

Consider a focussed probe formed by the first-order diffraction from an annular zone plate. The probe function will be given by the Fourier transform of the pupil function, and the far-field diffraction pattern of the probe will be given by the Fourier transform of the probe. We define the pupil function of the lens such that its far-field diffraction pattern, measured in the microdiffraction plane, is given by $A(\mathbf{r}')$. The maximum spatial frequency for which $A(\mathbf{r}')$ is non-zero is given by $\mathbf{r}'_{ZP} = NA/\lambda$, where NA is the numerical aperture of the zone plate and λ is the x-ray wavelength. The focal distribution of the zone plate is then given by the inverse

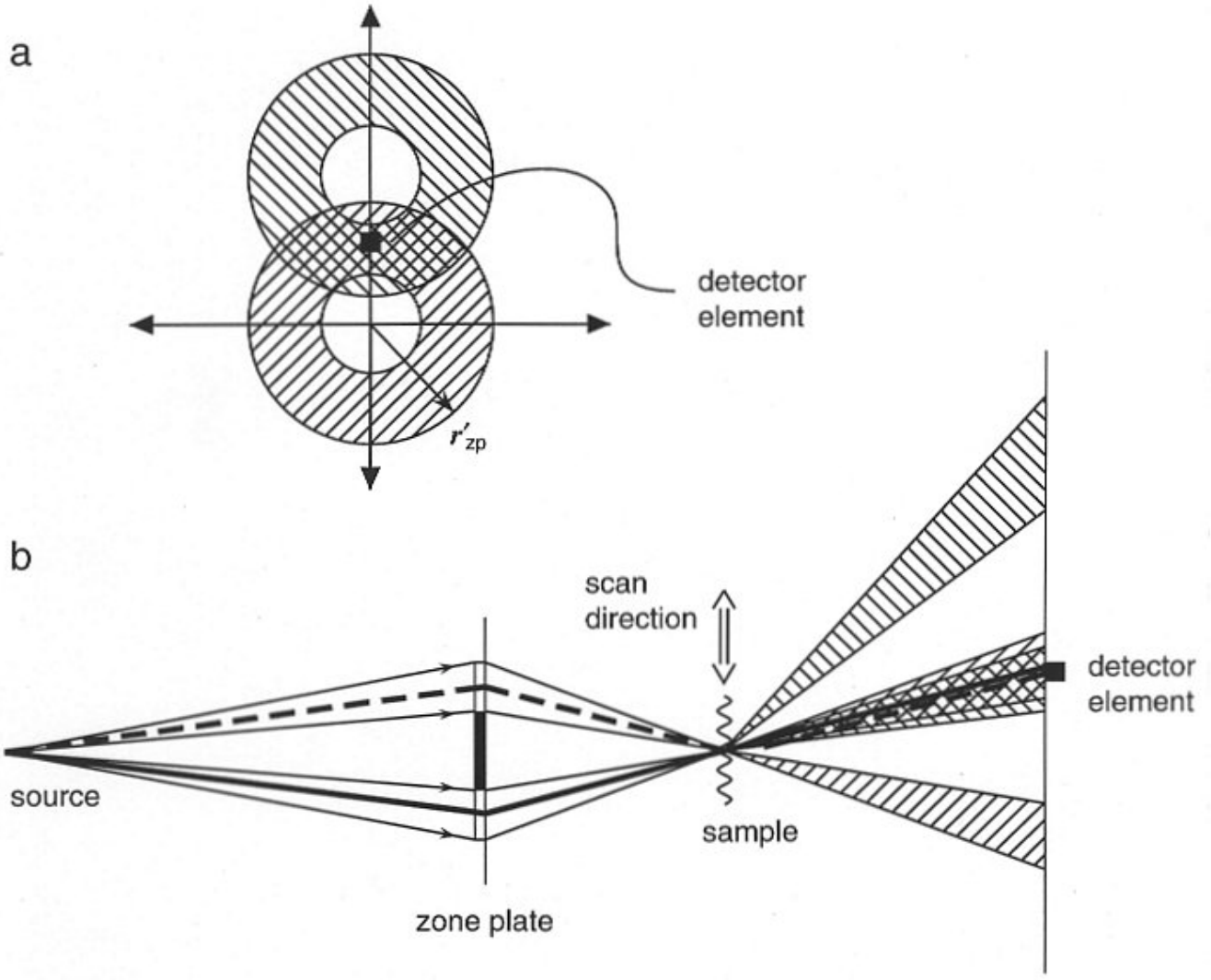

Figure 4. Schematic of diffraction by an object in the STXM. In this diagram it is assumed that a complex sinusoidal grating diffracts light only into zero and +1 orders. If the period is large enough so that the orders are separated by no more than $2r'_{ZP}$ then the diffracted pupil functions will overlap in the microdiffraction plane. A detector element in the region of overlap receives light that has travelled along two paths. This is actually a phase-shifting interferometer, where the phase shift is introduced by scanning the grating. The two paths are shown as the thick solid and thick dashed lines.

Fourier transform of *A*,

$$a(\mathbf{r}) = \mathfrak{F}_r^{-1}\{A(\mathbf{r}')\} \equiv \int A(\mathbf{r}')\exp(2\pi i\mathbf{r}'\cdot\mathbf{r})d\mathbf{r}' \qquad (1)$$

A specimen with complex transmission $\psi(\mathbf{r})$ is situated in the focal plane and scanned in that plane. At a given point in the scan the sample is displaced from the optical axis by a two-dimensional vector $-\mathbf{x}$. The x-ray wave-field immediately behind the specimen will then be given by $a(\mathbf{r})\psi(\mathbf{r}+\mathbf{x})$, and the intensity at the far-field microdiffraction plane, which is the modulus squared of the Fourier transform of this wavefield, can then be expressed as

$$m(\mathbf{r}',\mathbf{x}) = \left| \int A(\mathbf{r}'-\mathbf{s}')\,\Psi(\mathbf{s}')\exp(2\pi i\mathbf{s}'\cdot\mathbf{x})d\mathbf{s}' \right|^2 \qquad (2)$$

where Ψ is the Fourier transform of ψ, and the convolution integral is carried out over the entire microdiffraction plane; $\mathbf{s}'$ is the variable of integration.

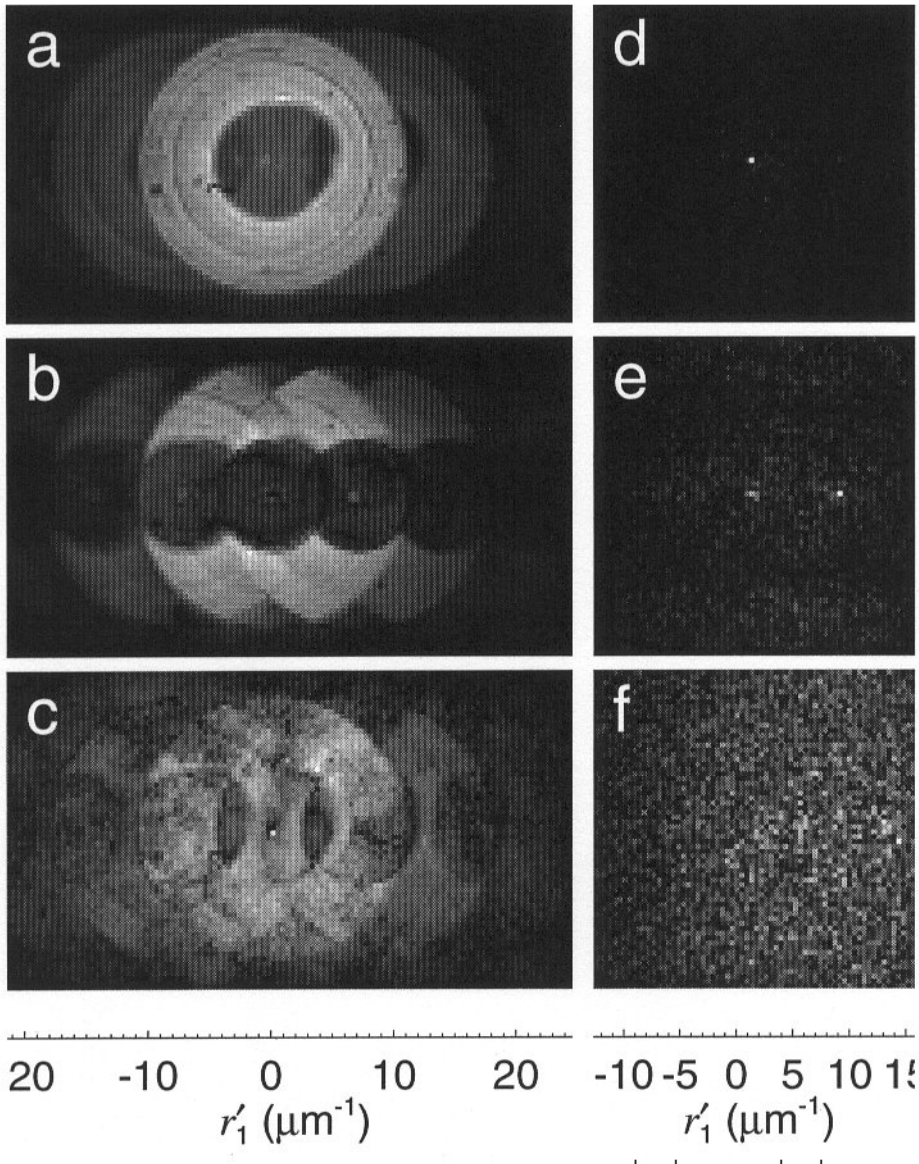

Figure 5. The amplitude of three $\mathbf{r}'$-planes of the distribution $M(\mathbf{r}',\mathbf{x}')$, for (**a**) $|\mathbf{x}'| = 0$, (**b**) $|\mathbf{x}'| = 6.85\ \mu m^{-1}$, and (**c**) $|\mathbf{x}'| = 10.3\ \mu m^{-1}$, showing the interference which occurs at these particular spatial frequencies as the grating is scanned, (**b**) shows the strong interference which occurs between the 0 and +1 orders, and the 0 and –1 orders, whereas. The results of deconvolving with the distribution $A(\mathbf{r}')A^*(\mathbf{r}'+\mathbf{x}')$ are shown in (**d**), (**e**), and (**f**). All images are displayed on a linear grey scale, but each has been individually scaled.

Scanning microscopy as phase-shifting interferometry

The intensity $m(\mathbf{r}',\mathbf{x})$ for constant $\mathbf{x}$ is a single microdiffraction pattern, recorded as a single frame of the CCD. Equation (2) shows that the convergent beam is diffracted by the object so that a pupil function $A(\mathbf{r}')$ is laid down at the microdiffraction plane, centred at each diffraction order of the specimen, and is multiplied by the complex amplitude of that diffraction order, $\Psi(\mathbf{s}')$. Each pupil function will also be multiplied by the "scanning phase factor", $\exp(2\pi\mathbf{s}'\cdot\mathbf{x})$, which is the phase shift induced in the diffracted beam due to the displacement of the object by $\mathbf{x}$. It is this scanning factor which provides the link between the real and reciprocal spaces and which provides the strong symmetry that exists in the data set between these two spaces (Chapman, 1996). In real space, the object $\psi(\mathbf{s})$ can be decomposed into complex sinusoidal gratings.

The grating of period $1/\mathbf{s}'$ has a complex amplitude $\Psi(\mathbf{s}')d\mathbf{s}'$ and diffracts radiation into the order at $\mathbf{s}'$ in reciprocal space. If the grating is shifted then the diffracted order will change phase accordingly. A shift by one period will change the phase of the order by 2π. Hence, a shift of the object by a vector $-\mathbf{x}$ will change the phases in all orders by different amounts, and the phase imposed on the order at $\mathbf{s}'$ will be $\exp(2\pi i\mathbf{s}'\cdot\mathbf{x})$.

The phase changes of the diffracted orders would have no effect on the measured intensity unless the orders may interfere with one another. The convergent beam illumination allows this to happen: two pupil functions laid down at two diffraction orders separated by $\Delta\mathbf{r}'$ will overlap if $|\Delta\mathbf{r}'| \leq 2r'_{ZP}$, as is the case in Figure 3a. As the object is scanned (i.e., as $\mathbf{x}$ is changed) the phases of the two orders will change, as described by the "scanning phase factor", and an intensity modulation will occur. The spatial frequency, $\mathbf{x}'$, of this modulation will be the difference of the frequencies of the two scanning phase factors, which is exactly $\Delta\mathbf{r}'$, the difference of the reciprocal vectors of the two orders. For the example of the transmission grating given above, the interference between the first order and zero order will modulate at the first-order frequency, as will the interference between the first and second orders. A coherent image formed by plotting the intensity recorded by a detector pixel in the overlap region between the zero and first orders, as a function of $\mathbf{x}$, will be a cosine function of exactly the first-order frequency. Such a coherent image from the experimental data set is shown in Figure 3b(i). The image is in fact the output of a phase-shifting interferometer drawn schematically in Figure 4. The phase of the intensity modulation depends on the phase of the object's first order diffracted wavefield relative to the zero order. It also depends on the relative phase of the two points in the pupil which the two beams passed through. Thus, if there is no phase variation across the pupil, or the pupil phase is known, then the phase of the object's first order can be found relative to its zero order.

The separability of the lens and object functions

In the example given in Figure 3 it was clear exactly which two diffraction orders caused the observed interference. For a general non-periodic object, the intensity at a given pixel in the microdiffraction detector will be usually caused by the interference of many diffraction frequencies (the coherent image formed from this detector pixel will be complicated and contain many frequencies). In this case each frequency, $\mathbf{x}'$, of the observed interference may be due to many different pairs of diffraction orders. However, as was seen above, each frequency of interference at any given detector pixel can only be due to pairs of object frequencies which differ by $\Delta\mathbf{r}' = \mathbf{x}'$. The interference due to any given pair of these frequencies will be distributed across the detector in a very specific area, namely the region of overlap of the two interfering pupils. Therefore, if we decompose the intensity recorded at each detector pixel into its spatial frequencies $\{\mathbf{x}'\}$, we will observe in $\mathbf{r}'$-space, for a constant $\mathbf{x}'$ only the areas of overlap of pupil functions which are separated by $\mathbf{x}'$. The pupil overlap function will be exactly the same shape for all these pairs of frequencies. However, the position of an overlap function in the $\mathbf{r}'$-plane depends on which pair of object frequencies gave rise to it. Thus, the distribution formed by taking the Fourier transform of the data set with respect to the scanning coordinate,

$$M(\mathbf{r}',\mathbf{x}') = \mathfrak{F}_x\{m(\mathbf{r}',\mathbf{x})\} \tag{3}$$

will be, for each $\mathbf{x}'$, given by the convolution of a specific pupil overlap function with all pairs of object frequencies which differ by $\mathbf{x}'$. This fact is strikingly illustrated in Figure 5, where planes of $M(\mathbf{r}',\mathbf{x}')$ for constant $\mathbf{x}'$ are shown for the transmission grating data set. The value of $\mathbf{x}'$ in Figure 5b is the first-order frequency of the grating, and it can be seen that specific frequencies of the scanned image are confined to particular regions of the microdiffraction plane.

Specifically, it can be shown (Rodenburg and Bates, 1992; Chapman, 1996) that the distribution M is given by

$$M(\mathbf{r}',\mathbf{x}') = [A(\mathbf{r}')A^*(\mathbf{r}'+\mathbf{x}')]\otimes'_r[\Psi(\mathbf{r}')\Psi^*(\mathbf{r}'-\mathbf{x}')] \tag{4}$$

where $\otimes'_r$ represents 2-d convolution with respect to the $\mathbf{r}'$ coordinate. The distribution $A(\mathbf{r}')A^*(\mathbf{r}'+\mathbf{x}')$ is the pupil overlap function which is non-zero only in the intersection between two pupil functions separated by $\mathbf{x}'$.

Deconvolving the data set

If A is well known then the pupil overlap function of Equation (4) can be computed and deconvolved from each $\mathbf{r}'$-plane of $M(\mathbf{r}',\mathbf{x}')$. Deconvolution involves Fourier transforming the convolution to form a product, so the processing of the data requires the step

$$\begin{aligned} M(\mathbf{r},\mathbf{x}') &\equiv \mathfrak{F}_r^{-1}\{M(\mathbf{r}',\mathbf{x}')\} \\ &= \mathfrak{F}_r^{-1}\{A(\mathbf{r}')A^*(\mathbf{r}'+\mathbf{x}')\}\,\mathfrak{F}_r^{-1}\{\Psi(\mathbf{r}')\Psi^*(\mathbf{r}'-\mathbf{x}')\} \end{aligned} \tag{5}$$

which follows from Equation (4) by the convolution theorem. The terms in Equation (5) are in fact Wigner distribution functions (WDFs) or, more precisely, ambiguity functions (Cohen, 1989). The definition and some properties of WDFs are given in Table 1, from which it can be seen that

$$M(\mathbf{r},\mathbf{x}') = W_a(\mathbf{r},-\mathbf{x}')W_\Psi(\mathbf{r},\mathbf{x}') \tag{6}$$

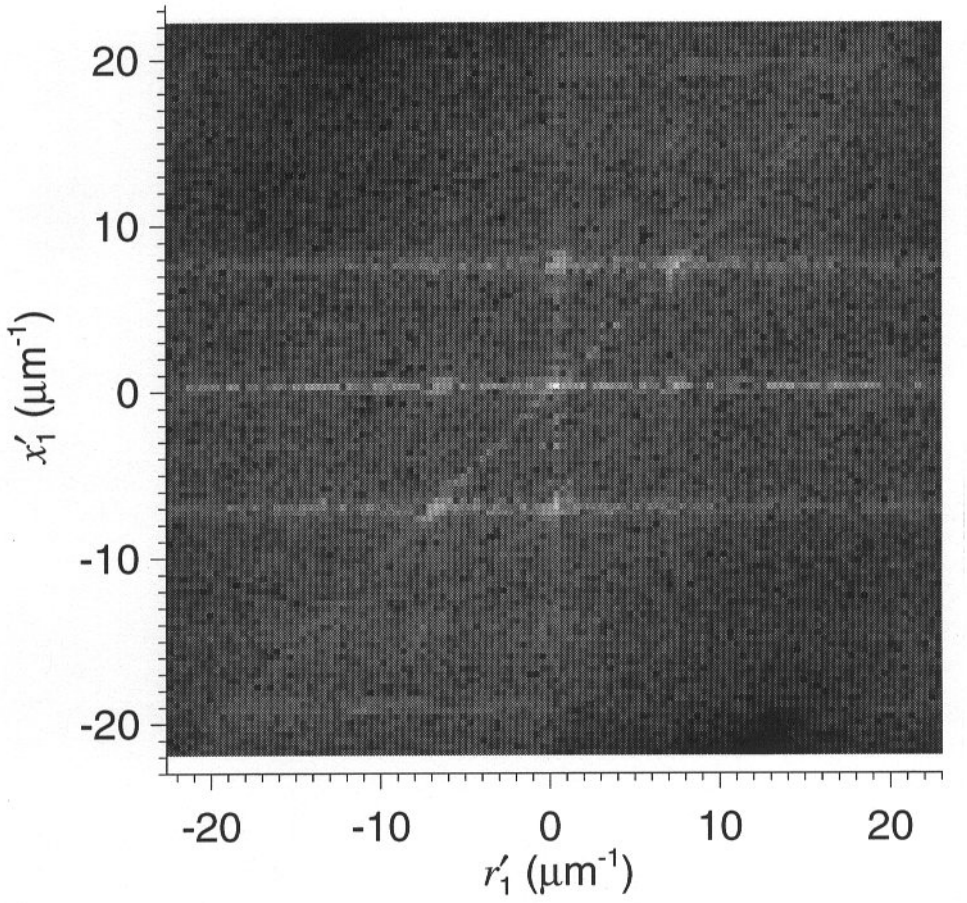

Figure 6. The amplitude of a 2-d plane of the local autocorrelation distribution of the grating object's spectrum, $\Psi(r_1')\Psi^*(r_1'-x_1')$, found by Wigner deconvolution. Each row of this image is the $r_2'=0$ row of the deconvolution for each value of x_1'. Columns of the array give displaced estimates of the complex angular spectrum of the grating. No interference can occur for $|\Delta\mathbf{r}'| > 22.2\ \mu m^{-1}$. The amplitude is displayed here at low contrast (gamma of 0.2).

---

where W_f is the WDF of function f.

Since the WDF W_a contains zeroes and regions of low signal to noise, the deconvolution is best performed using a Wiener filter (Bates and McDonnel, 1986). That is, an estimate, $_\Psi$, of the WDF of the specimen is given by

$$_\Psi(\mathbf{r},\mathbf{x}') = M(\mathbf{r},\mathbf{x}')\,T(\mathbf{r},\mathbf{x}') \qquad (7)$$

where

$$T(\mathbf{r},\mathbf{x}') = [W_a^*(\mathbf{r},-\mathbf{x}']/[\,|W_a(\mathbf{r},-\mathbf{x}')|^2 + \phi_a] \qquad (8)$$

and ϕ_a is a small constant. Fourier transforming $_\Psi$ with respect to $\mathbf{r}$ will yield estimates of the relative amplitudes and phases of pairs of object frequencies differing by $\mathbf{x}'$, $\Psi(\mathbf{r}')\Psi^*(\mathbf{r}'-\mathbf{x}')$, referred to as the local autocorrelation distribution of Ψ.

The deconvolution of the example grating data has been carried out for each $\mathbf{r}'$-plane of $M(\mathbf{r}',\mathbf{x}')$. The result at $|\mathbf{x}'|$ is shown in Figure 5e. The two most noticeable features of the deconvolution are two delta functions. One is located at $\mathbf{r}' = 0$, and is thus due to the interference between the zero-order and the –1 order. The other is located at approximately $|\mathbf{r}'| = 6.85\ \mu m^{-1}$ and is due to the interference between the +1 and zero orders. Note that since the microdiffraction data set is real, the transformed planes at

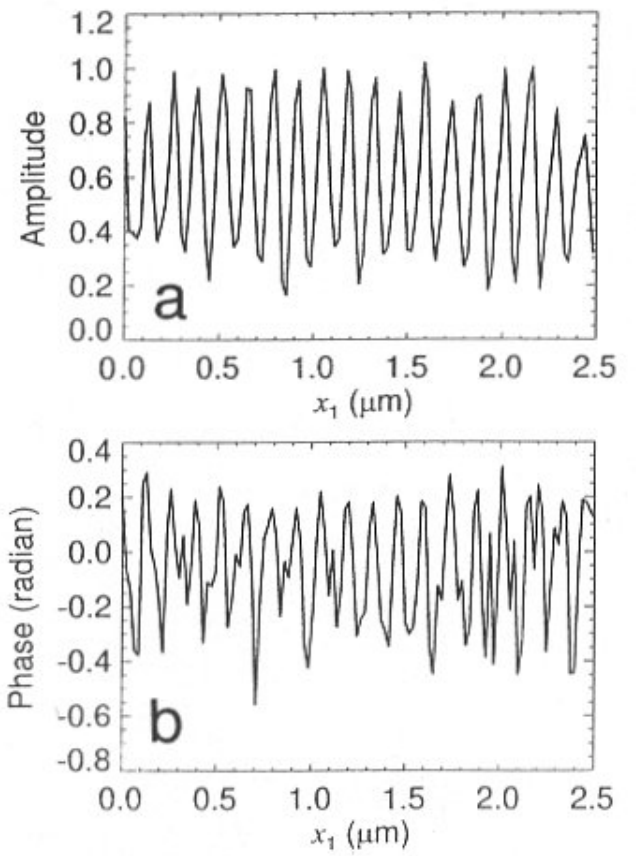

Figure 7. The retrieved amplitude (**a**) and phase (**b**) of the transmission grating, formed by phasing the interference within the zero-order pupil.

$\pm\mathbf{x}'$ will be identical. However, the procedure deconvolves these planes with pupil overlap functions which differ from each other by a shift (see Eqn. 4), so the delta function located at $\mathbf{r}' = 0$ in the deconvolution at $|\mathbf{x}'| = 6.85\ \mu m^{-1}$ will give the phase and amplitude of the interference between the +1 and 0 orders.

A two-dimensional slice of the deconvolved distribution $\Psi(\mathbf{r}')\Psi^*(\mathbf{r}'-\mathbf{x}')$ is shown in Figure 6. This plane is formed by taking the line of each deconvolution at r'_2. It is seen that there are three main orders (–1, 0, and +1) and the relative phase and amplitude of each of seven combinations of pairs of these orders can be seen in the distribution. (The interference of –1 with +1 cannot easily be observed.) Since the grating is not perfect and does contain a continuous set of spatial frequencies, lines can be observed in Figure 6 where interference occurs between these frequencies and the stronger diffraction orders. These are the faint vertical and diagonal lines. The horizontal lines

Table 1. Properties of the Wigner-distribution function (WDF), W_f. As defined here the distribution is formally known as an ambiguity function, and differs from a Wigner-Ville distribution (Classen and Mecklenbrüker, 1980) by a coordinate transformation and a phase term. As with most space - spatial frequency distributions, the WDF is formed by Fourier transforming a self-overlap distribution of a function, called a local autocorrelation distribution. For a more complete description see Cohen (1989). Note that in the last equation, the 4D transform $\mathfrak{F}_x^{-1}\mathfrak{F}_r$ rotates the distribution in 4-space.

$$W_f(\mathbf{r},\mathbf{x}') \equiv \int f^*(\mathbf{x})\, f(\mathbf{x}+\mathbf{r}) \exp(-2\pi i \mathbf{x}\cdot\mathbf{x}')d\mathbf{x} = \int F(\mathbf{r}')F^*(\mathbf{r}'-\mathbf{x}') \exp(2\pi i \mathbf{r}\cdot\mathbf{r}')d\mathbf{r}' \quad \text{(a)}$$

$$w_f(\mathbf{r},\mathbf{x}) \equiv \mathfrak{F}_x^{-1}\{W_f(\mathbf{r},\mathbf{x}')\} = f^*(\mathbf{x})f(\mathbf{x}+\mathbf{r}) \quad \text{(b)}$$

$$w_f^*(\mathbf{r},-\mathbf{x}) = \mathfrak{F}_x\{W_f(\mathbf{r},\mathbf{x}')\} = f(-\mathbf{x})f^*(-\mathbf{x}+\mathbf{r}) \quad \text{(c)}$$

$$W_f(\mathbf{r}',\mathbf{x}') \equiv \mathfrak{F}_r\{W_f(\mathbf{r},\mathbf{x}')\} = F(\mathbf{r}')F^*(\mathbf{r}'-\mathbf{x}') \quad \text{(d)}$$

$$W_f^*(-\mathbf{r}',\mathbf{x}') = \mathfrak{F}_r^{-1}\{W_f(\mathbf{r},\mathbf{x}')\} = F^*(-\mathbf{r}')F(-\mathbf{r}'-\mathbf{x}') \quad \text{(e)}$$

$$\mathfrak{F}_x^{-1}\mathfrak{F}_r\{W_f(\mathbf{r},\mathbf{x}')\} = \int F(\mathbf{r}')F^*(\mathbf{r}'-\mathbf{x}') \exp(2\pi i \mathbf{x}\cdot\mathbf{x}')d\mathbf{x}' = W_f(\mathbf{x},\mathbf{r}') \quad \text{(f)}$$

are due to errors in the deconvolution (for example, due to a phase error on the zone-plate pupil) and occur in planes of constant $\mathbf{x}'$ where there is high power.

The complex spatial-frequency spectrum of the object is extracted frequency by frequency from each deconvolved plane at $\mathbf{r}' = 0$, for values of $|\Delta\mathbf{r}'| \le 2r'_{ZP}$ (a resolution of 22.2 μm^{-1}, or 45.0 nm). This can be immediately transformed to give the complex image as shown in Figure 7.

Deconvolving Sampled Data

As has been seen in previous sections, the measured data set is a continuous distribution that has been sampled in all four dimensions. The implications of this fact on deconvolving the data set are discussed here, as well as suggestions of what sampling intervals should be used to record the data set. It will be assumed for this discussion that every **x**- or $\mathbf{r}'$-plane is sampled on a square grid with square pixels. It is trivial to generalise to grids with different spacings and numbers of samples in each dimension. The sample stage is raster-scanned and stepped by increments Δx in the orthogonal x_1 and x_2 directions between CCD readouts. Each microdiffraction plane is recorded by the pixellated CCD detector. It is assumed that each pixel detects photons in a square area with a width the same as the pixel

spacing. That is, there is no dead area between pixels. (This is a reasonable assumption for back illumination with x-rays.) In some cases the CCD pixels are binned into square or rectangular regions, each region giving the summation of intensity in several pixels. The recorded microdiffraction pattern is the actual pattern integrated over square "areas" of reciprocal space of width $\Delta r'$, spaced by the same width. The recorded pattern is therefore the convolution of the diffraction pattern and the pixel shape, *P*, as

$$m^p(\mathbf{r}',\mathbf{x}) = m(\mathbf{r}',\mathbf{x}) \otimes P(\mathbf{r}') \tag{9}$$

sampled on the grid defined by

$$\mathbf{r}' = \Delta r' \mathbf{j}_r; \qquad \mathbf{x} = \Delta x \mathbf{j}_x \tag{10}$$

Here, $\mathbf{j}_r$ and $\mathbf{j}_x$ are the two-dimensional indices, with $N_r \times N_r$ and $N_x \times N_x$ samples respectively. We define the index-arrays to have integer values from $-N/2 + 1$ to $N/2$ in each dimension, where *N* is the number of samples in that dimension. Thus, the real-space origin and the zero spatial frequency are located in the centre of the arrays.

The data sets are processed numerically using fast Fourier transforms (FFTs) to compute the complex, discrete Fourier transform. By the Shannon sampling theorem (Bracewell, 1986) the set of transforms of the coherent images, $M(\mathbf{r}',\mathbf{x}')$, is sampled in the $\mathbf{x}'$-planes on the grid

$$\mathbf{x}' = \Delta x' \mathbf{j}_x, \text{ with } \Delta x' = 1/(N_x \Delta x) \tag{11}$$

and the maximum frequencies that can be sampled in each dimension of the x-planes is given by

$$x'_{max} = \Delta x' N_x/2 = 1/(2\Delta x) \tag{12}$$

A similar relationship holds for r'_{max}, the maximum spatial frequency recorded in each microdiffraction plane.

The sampling interval Δx can be varied by changing the step size of the scanning actuators, whereas $\Delta x'$ can be chosen by selecting the x-ray wavelength, the CCD-sample distance, or the binning of detector elements on the CCD.

In the STXM the best choice of the sampling intervals depends on the desired resolution and field size of the final reconstructed image, and the resolution of the zone-plate. Given a zone plate of numerical aperture $\lambda r'_{ZP}$, the maximum frequency of modulation in the microdiffraction plane, as the sample is scanned, will be the maximum separation of two intersecting pupil functions, which is $2r'_{ZP}$. The maximum frequency, x'_{max}, required for the scanning stage need not be greater than $2r'_{ZP}$, since there will be no data for higher values of x'. Therefore, by Equation (12), the smallest scanning-stage step size would be $\Delta x = 1/(4r'_{ZP})$. By the "stepping out" method of Rodenburg and Bates (1992), images can be reconstructed at resolutions higher than $2r'_{ZP}$ by phasing interference at positions in the microdiffraction plane at $r' > 2r'_{ZP}$. The choice of r'_{max} will depend on the extent of diffracted intensity that can be recorded, which in turn will depend on the dynamic range of the detector and the x-ray dose that can be tolerated by the sample. For weakly-scattering objects, the interference will predominantly occur within the zero-frequency pupil, so there would not be much point in recording beyond $r' = 2r'_{ZP}$. However, to achieve superresolved reconstructions from more strongly scattering samples, considerably larger values of r'_{max} should be chosen.

The number of samples in all four dimensions will depend on what image field is desired in a single reconstruction. The field width of the scanning stage is $N_x \Delta x$. The field width also determines the conjugate sampling interval, since $\Delta x' = 1/(N_x \Delta x)$. The number of samples in the CCD should be chosen so that the sampling interval $\Delta r'$ is approximately equal to $\Delta x'$. If $\Delta r' \gg \Delta x'$ then the interval $\Delta x'$ will be too small to give any appreciable change between consecutive $\mathbf{r}'$-planes. With the typical large amplitude variations across the pupil of zone plates, there may be a risk of aliasing if $\Delta x'$ is chosen to be too small. If, on the other hand, $\Delta r' \ll \Delta x'$ then each microdiffraction plane will be over-sampled. This may improve the accuracy of the deconvolution, but at the expense of collecting a much greater amount of data.

The deconvolution proceeds by applying the Wiener filter of Equation (8). The filter is a function of the Wigner Distribution of the zone-plate pupil, calculated from the pupil overlap functions for each value of $\mathbf{x}'$. Due to the large non-uniformities in the amplitude of the zone-plate pupil a direct measurement of the pupil is used rather than a modelled function. The pupil amplitude is taken as the square root of the measured microdiffraction intensity when no object is placed in the beam (Fig. 2), and the pupil phase is usually assumed to be zero. Since it has not been possible in practice to acquire data with $\Delta r'$ exactly equal to $\Delta x'$, the pupil intensity is measured on the entire CCD array without any pixel binning (i.e., with 512×512 pixels). The actual microdiffraction data set is usually collected with much less samples per diffraction plane and the detector elements binned into 4×4 or 8×8 groups. Therefore the pupil measurement is over-sampled relative to the data set, allowing pupil overlap functions to be calculated for pupil shifts that are not integer multiples of $\Delta r'$. The pupil overlap functions are computed from the over-sampled array, with

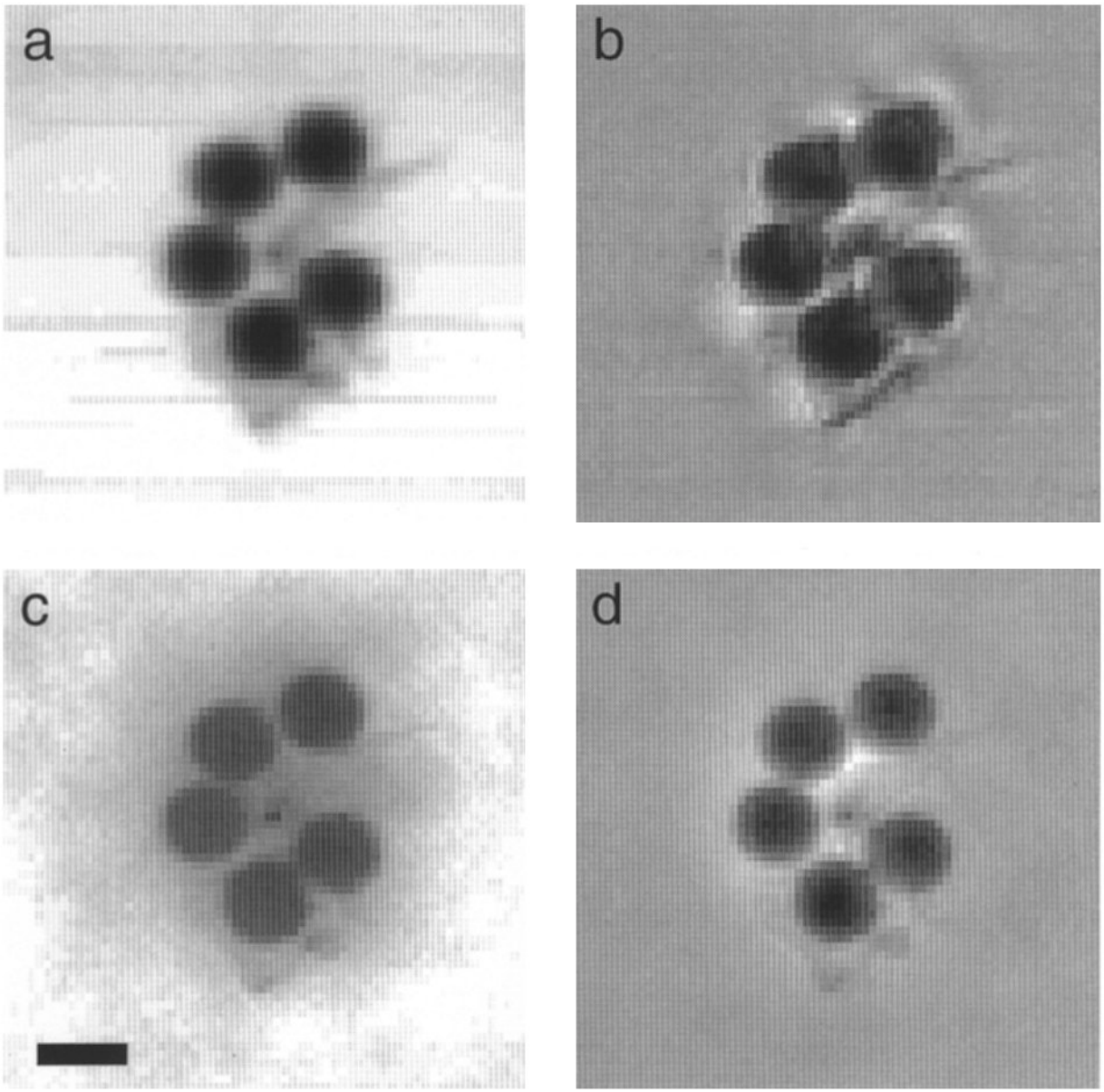

Figure 8. Images obtained from a microdiffraction data set recorded at an x-ray wavelength of 3.1 nm, for an object consisting of a group of latex particles. (**a**) The incoherent bright-field image (white = 1.0 intensity transmission, black = 0.3). (**b**) The coherent bright-field image formed at $\mathbf{r}' = (4.53, 5.44)\ \mu m^{-1}$, displayed with a greyscale ranging from 0.15 to 1.3. The amplitude (**c**) and phase (**d**) of the retrieved complex transmission of the specimen, taken from the deconvolved WDF at $\mathbf{r}' = 0$. In (**c**), white = 0 and black = 1.0, and in (**d**), white = 0.5 rad and black = –1.5 rad. The scalebar represents 0.5 μm.

---

the shift, $\mathbf{x}'$, for each $\mathbf{r}'$-plane rounded off to the nearest pixel value of the over-sampled array. Each product is then sampled onto the same grids as the experimental data by nearest-neighbour averaging. The calibration between the sampling intervals of the scan and microdiffraction coordinates is made by optimising the deconvolution of a single $\mathbf{r}'$-plane of $M(\mathbf{r}',\mathbf{x}')$ with a pupil overlap function calculated for various values of $\mathbf{x}'$. Generally the optimisation procedure involves checking that the deconvolution yields numerical results in agreement with the summation over regions of the microdiffraction plane

(such as over the zero-order pupil), and that the noise in the deconvolution is at a minimum.

For large amounts of over-sampling of the pupil measurement relative to the data set, this nearest-neighbour averaging is approximately equivalent to the convolution of unsampled data with the pixel shape function *P*, of Equation (9). Therefore there is no need to make additional corrections for the pixel shape in the microdiffraction data set.

The Wiener filter of Equation (8) requires a value for the parameter ϕ_a. The noisier the data, the larger ϕ_a should be, in order to limit the amplification of noise. The choice of the parameter is made by first optimising the deconvolution of several $\mathbf{r}'$-planes of $M(\mathbf{r}',\mathbf{x}')$.

The actual algorithm used to retrieve the phase of images of specimens has be implemented in the IDL programming language, which is an interpreted language that has built-in low-level routines for operating on arrays. Running on an IBM RS/6000, with 64 Mbytes of RAM, a 4D (four-dimensional) Fourier transform of a 32×32×64×64 complex array [as is needed to calculate $M(\mathbf{r},\mathbf{x}')$ for example] takes approximately 15 minutes. Transforms of larger arrays cannot be achieved within the 64 Mbyte memory, so blocks of data must be transferred between RAM and a fixed disk. A 64^4 4D transform therefore takes about 2.5 hours, instead of 1.4 hours as would be expected from $N \log N$ scaling.

Phase-Retrieved Image of a Non-Periodic Object

An example of a phase-retrieved image of a non-periodic object is presented here to demonstrate the use of the algorithm and its implementation on x-ray data collected in the STXM. The retrieved phase and amplitude images of a group of 0.5-μm-diameter latex spheres is shown in Figure 8. The images were generated from a microdiffraction data set consisting of 64×64 real-space samples at 45-nm intervals, and 64×64 reciprocal-space samples at 0.8-μm^{-1} intervals. The x-ray wavelength was 3.1 nm, and the exit slit of the beamline monochromator was set to give approximately 70% spatial coherence across the diameter of the zone plate. The incoherent bright-field image, $\int m(\mathbf{r}',\mathbf{x})d\mathbf{r}'$, is shown in Figure 8a, and one particular coherent bright-field image is shown in Figure 8b. The coherent image formed at each CCD detector pixel was Fourier transformed, to form the distribution $M(\mathbf{r}',\mathbf{x}')$. Each $\mathbf{r}'$-plane of $M(\mathbf{r}',\mathbf{x}')$ was deconvolved with the appropriate pupil-overlap function, and an estimate of the transform of the object local autocorrelation was built up plane by plane. The object's complex angular spectrum was extracted from the orthogonal plane at $\mathbf{r}' = 0$ (this was the only region of high-signal data since the object′s transform is dominated by the zero order), and then transformed to give the complex image shown in Figure 8c (amplitude), and 8d (phase).

It is interesting to note that the phase image displays very little noise, whereas the retrieved amplitude image has about the same level of noise as the coherent bright-field image. Given that there were 454 detector samples made within the zero-order pupil, the signal to noise ratio (SNR) of the incoherent bright-field should be 21 times the SNR of any one of the coherent bright-field images the image. Assuming that the retrieved image does have the same noise level as a coherent image, then the dose required to obtain phase-retrieved images is also about 21 times that to obtain incoherent bright-field images at the same SNR.

A quantitative characterisation of phase-retrieval x-ray microscopy has been carried out (Chapman, 1996) by imaging an isolated single latex sphere. In that study it was found that the retrieved phase was in excellent agreement with theoretical calculations (within 5%). However, estimates of the object's amplitude, acquired from two orthogonal planes of the 4D deconvolved distribution, were not in agreement. That is, the deconvolved distribution could not self-consistently be described as a Wigner distribution, and it was found that the reason for this was that the estimate of the pupil phase used in the deconvolution was incorrect. Since the complex transmission of the isolated sphere could be very accurately modelled, the complex pupil function could be retrieved by deconvolving the Wigner distribution function of the modelled object from the microdiffraction data set. In this case the deconvolution gave rise to self-consistent object and pupil distributions. In addition, a comparison of the retrieved pupil amplitude with the measured amplitude gave information about the mutual coherence of the beam incident on the zone plate. The retrieved pupil phase (i.e., the zone-plate aberrations), the measured pupil amplitude, and the beam coherence, completely characterised the x-ray microscope. Subsequent deconvolutions of microdiffraction data sets collected from test objects were found to be in good agreement with theoretical calculations.

Summary and Discussion

The phase-retrieval method of Wigner Distribution deconvolution, which has before been carried out using visible light and electrons, has been successfully demonstrated with soft x-rays. The method finds the relative amplitude and phase of all pairs of interfering diffraction orders of the object. For typical specimens examined in the x-ray microscope, zero-order diffraction dominates, and the phase-retrieved image is obtained from the interference occurring within the zero-order beam at the microdiffraction plane (i.e., to a resolution of 45 nm with the zone plates used here). The method was used to find the amplitude and

phase of periodic and non-periodic specimens alike. The phases of the images are retrieved at an accuracy of about 0.05 rad, and the amplitudes are found to less than 10% from the incoherent bright-field images. (The incoherent bright-field image is extracted from the same microdiffraction data set as the phase information.)

The deconvolution process is extremely robust due to the overdetermined nature of the data set. In the examples presented here it was not necessary to accurately know the phase of the zone plate pupil to acquire accurate phase maps. Other instrument properties which could have affected the ability of the reconstruction algorithm, such as specimen drift, non-object scatter, detector inhomogeneities, and noise in the scanning stage, were either at a low enough level not to be important, or could be accounted for in the measurements. The coherence of the x-ray beam illuminating the zone plate was high enough (70% for light at the edge of the zone plate interfering with light at the centre) so that this did not have to be accounted for.

Phase-retrieval x-ray microscopy by Wigner distribution deconvolution should find much utility in accurately determining the ultrastructure of biological and materials science specimens. The phase information may visualise structures that could not be seen before, or help identify image features. Near x-ray absorption edges, where the real and imaginary parts of the refractive index can vary very strongly depending on the chemical environment, the additional phase information will be very useful. Wigner deconvolution microscopy also provides a way of accurately measuring the soft-x-ray optical constants of materials, which are not well known in the 100–700 eV range, due to a lack of interferometers that operate at these energies. Phase-retrieval microscopy should also be useful at hard x-ray energies. At present, hard-x-ray STXMs are under development at the new high-brightness, high-energy synchrotrons, and Wigner-deconvolution would be a very useful technique for the study of crystallites in such instruments. Even though the numerical aperture of 10 keV zone plates is extremely small, the relative phases of diffraction peaks that are closely separated could easily be measured. This may aid in the identification of microcrystals in a sample, or even help in the structure determination of crystals. At the harder x-ray wavelengths, the phase shift dominates, making the availability of an accurate phase imaging method very important.

Acknowledgements

I would like to thank Janos Kirz and Chris Jacobsen of the Department of Physics, SUNY at Stony Brook, for much help and many stimulating discussions. Sue Wirick (Physics, SUNY at Stony Brook) has offered a lot of technical assistance. I also thank John Rodenburg, University of Cambridge, for his correspondence and advice; and Erik Anderson (Lawrence Berkeley National Lab), who fabricated the zone plates used in this study. This work was supported by the Department of Energy (DoE) under grant number FG02-89ER60858, and was performed in part at the National Synchrotron Light Source, which is supported by the DoE office of Basic Energy Sciences.

References

Anderson E, Kern D (1992) Nanofabrication of zone plate lenses for high resolution X-ray microscopy. In: X-ray microscopy III. Michette AG, Morrison GR, Buckley CJ (eds). Springer Series in Optical Sciences, vol. 67. Springer, Berlin. pp 75–78.

Bates RHT, McDonnel MJ (1986) Image restoration and reconstruction, Clarendon, Oxford.

Bates RHT, Rodenburg JM (1989) Sub-Ångström transmission microscopy: a Fourier transform algorithm for microdiffraction plane intensity information. Ultramicroscopy **31**: 303–308.

Bracewell RN (1986) The Fourier transform and its applications, 2nd ed., McGraw-Hill, New York.

Chapman HN (1996) Phase-retrieval X-ray microscopy by Wigner-distribution deconvolution. Ultramicroscopy **66**: 153-172.

Chapman HN, Jacobsen C, Williams S (1995) Applications of a CCD detector in a scanning transmission x-ray microscope. Rev Sci Instrum **66**: 1332–1334.

Chapman HN, Jacobsen C, Williams S (1996) A characterisation of dark-field imaging of colloidal gold labels in a scanning transmission x-ray microscope. Ultramicroscopy **62**: 191-213.

Classen TACM, Mecklenbrüker WFG (1980) The Wigner distribution – A tool for time-frequency signal analysis: Part III – Relationship with other time-frequency signal transformations. Philips J Res **35**: 372– 389 (1980).

Cohen L (1989) Time-frequency distributions – a review. Proc IEEE **77**: 941–981.

Jacobsen C, Williams S, Anderson E, Browne MT, Buckley CJ, Kern D, Kirz J, Rivers M, Zhang X (1991) Diffraction limited imaging in a scanning transmission x-ray microscope. Opt Comm **86**: 351–364.

Jacobsen C, Lindaas S, Williams S, Zhang X (1993) Scanning luminescence x-ray microscopy: imaging fluorescence dyes at sub-optical resolution. J Microsc **172**: 121–129.

Jacobsen C, Anderson E, Chapman H, Kirz J, Lindaas S, Rivers M, Wang S, Williams S, Wirick S, Zhang X (1994) The X-1A scanning transmission X-ray microscope: optics and instrumentation. In: X-ray Microscopy IV. Aristov VV, Erko AI (eds). Bogorodski Pechatnik. pp 304-321.

Kirz J, Jacobsen C, Howells M (1995) Soft X-ray

microscopes and their biological applications. Q Rev Biophys **28**: 33–130.

McCallum BC, Rodenburg JM (1992) Two-dimensional demonstration of Wigner phase-retrieval microscopy in the STEM configuration. Ultramicroscopy **45**: 371–380.

Morrison GR, Browne MT (1992) Dark-field imaging with the scanning transmission x-ray microscope. Rev Sci Instrum **63**; 611–614.

Nellist PD, Rodenburg JM (1994) Beyond the conventional information limit: the relevant coherence function. Ultramicroscopy **54**: 61–74 (1994).

Nellist PD, McCallum BC, Rodenburg JM (1995) Resolution beyond the "information limit" in transmission electron microscopy. Nature **374**: 630 –632.

Palmer JR, Morrison GR (1992) Differential phase contrast in x-ray microscopy. In: X-ray microscopy III. Michette AG, Morrison GR, Buckley CJ (eds). Springer Series in Optical Sciences, vol. 67. Springer, Berlin. pp. 278–280.

Rarback H, Buckley C, Ade H, Camilo R, DiGennaro R, Hellman S, Howells M, Iskander N, Jacobsen C, Kirz J, Krinsky S, Lindaas S, McNulty I, Oversluizen M, Rothman S, Sayre D, Sharnoff M, Shu D (1990) Coherent radiation of X-ray imaging - the soft X-ray undulator and the X1A beamline at the NSLS. J Vac Sci Tech **2**: 274-296.

Rodenburg JM, Bates RHT (1992) The theory of super-resolution electron microscopy via Wigner-distribution deconvolution. Phil Trans R Soc Lond A **339**: 521–553.

Rodenburg JM, McCallum BC, Nellist PD (1993) Experimental tests on double-resolution coherent imaging via STEM. Ultramicroscopy **48**: 304–314.

Tejnil E, Goldberg KA, Bokor J, Anderson EH (1996) Zonal placement errors in zone plate lenses. In: Extreme Ultraviolet Lithography, OSA Technical Digest (Optical Society of America, Washington DC), pp 50–52.

Thieme J, David C, Fay N, Kaulich B, Medenwaldt R, Hettwer M, Guttmann P, Kögler U, Maser J, Schneider G, Rudolph D, Schmahl G (1994) Zone plates for high resolution x-ray microscopy. In: X-ray Microscopy IV. Aristov VV, Erko AI (eds). Bogorodski Pechatnik, pp 487–493.

Von Brenndorff AI, Moronne MM, Larabell C, Selvin P, Meyer-Ilse W (1994) Soft x-ray stimulated high resolution luminescence microscopy. In: X-ray Microscopy IV. Aristov VV, Erko AI (eds). Bogorodski Pechatnik. pp 337–343.